

Electronic Supplementary Material (ESI) for Journal of Materials Chemistry A.

This journal is © The Royal Society of Chemistry 20XX

Electronic Supplementary Information

Heteroatoms doped Graphdiyne as High Efficient Electrocatalyst for Oxygen Reduction Reaction in Alkaline Medium

Shuangshuang Zhang,^{a,d} Yingjun Cai,^a Hongyan He,^a Yaqin Zhang,^{a,d} Rongji Liu,^a Hongbin Cao,^a
Meng Wang,^{a,d} Jingjing Liu,^{a,e} Guangjin Zhang,^{*a} Yuliang Li,^b Huibiao Liu^b and Bin Li^{*c}

^a*Key Laboratory of Green Process and Engineering, Institute of Process Engineering, Chinese
Academy of Sciences, 100190, Beijing, China*

^b*Institute of Chemistry, Chinese Academy of Sciences, 100190, Beijing, China*

^c*Zhengzhou Tobacco Research Institute of CNTC, 450001, Zhengzhou, China*

^d*University of Chinese Academy of Sciences, 100039, Beijing, China*

^e*Beijing University of Chemical Technology, 100029, Beijing, China*

E-mail: zhanggj@ipe.ac.cn ; lib@ztri.com.cn

Experimental details:

Materials: Anhydrous zinc chloride (ZnCl_2), boron oxide (B_2O_3), ammonium fluoride (NH_4F), thiourea, Pt/C (Pt 20% mass loading on carbon black) and poly-tetrafluoroethylene (PTFE, 60% PTFE in water) were purchased from Alfa Aesar Company and used as received. Active carbon was purchased from Sigma Aldrich. 5% Nafion (purchased from Sigma Aldrich) were dissolved in isopropyl alcohol to get the 0.1% Nafion to use. The other reagents were of analytical purity and were used without further purification.

Structure characterizations: XPS measurements were carried out on an ESCALAB250Xi apparatus at base pressure of 1×10^{-9} mbar, and X-ray source of Al $K\alpha$. TEM images were got from a JEM-2100 (UHL) transmission electron microscope at an acceleration voltage of 200kV. The FESEM and elemental mapping images were performed on a SU8020 field emission scanning electron microscope. The Raman spectra were obtained with a Renishaw Raman System Model 1000 spectrometer. The 532 nm radiation from a 20mW air-cooled argon ion laser was used as the exciting source. The laser diameter was $1 \mu\text{m}$ and the laser power at the sample position was 4.0 mW. Powder XRD studies were recorded on a Bruker AXS D advance powder diffractometer with a Cu $K\alpha$ ($\lambda = 0.15418$ nm). Nitrogen adsorption/desorption measurements were performed at 77 K using a Quantachrome Autosorb- iQ-MP gas-sorption system.

Conductivity measurements of GD-based materials: The electrochemical impedance spectra (EIS) were obtained from a ZAHNER ZENNIUM electrochemical workstation (ZAHNER Instrument Inc., Germany) in the presence of a 1 mM $\text{K}_3[\text{Fe}(\text{CN})_6]/\text{K}_4[\text{Fe}(\text{CN})_6]$ (1:1, mol/mol) mixture as a redox probe in 0.1 M KCl aqueous solution. The frequency range was 100 000~0.01Hz with a

signal amplitude of 5 mV.

Oxygen Reduction Reaction (ORR) Measurements:

Cyclic voltammetry (CV) testing: CV was conducted in a home-made electrochemical cell. The electrolyte (0.1 M KOH) was saturated with oxygen by bubbling O₂ for at least 30 minutes before the measurements. During the recording of CVs, a flow of O₂ was maintained over the electrolyte to ensure its continued O₂ saturation. The working electrode was cycled for 5 times before the data were recorded. The voltage range of CVs was from -0.05 V to 1.15 V vs. RHE, with the sweep rate of 10 mV s⁻¹. In the control experiments, CVs were performed in an Ar-saturated 0.1 M KOH.

Rotating disk electrode (RDE) measurements: The working electrode was scanned at a rate of 10 mV s⁻¹ with rotating speeds from 400 rpm to 1600 rpm. Koutecky–Levich (K-L) plots (J^{-1} vs. $\omega^{-1/2}$) were analysed at various electrode potentials. The slopes of the linear lines were used to calculate the electron transfer numbers (n) on the base of the following K-L equations:

$$\frac{1}{J} = \frac{1}{J_L} + \frac{1}{J_K} = \frac{1}{B\omega^{1/2}} + \frac{1}{J_K} \quad (1)$$

$$B = 0.2nFC_{O_2}(D_{O_2})^{2/3}\nu^{-1/6} \quad (2)$$

Where J is the measured current density, J_K and J_L are the kinetic- and diffusion-limiting current densities, B is the reciprocal of the slope, ω is the angular velocity, F is the Faraday constant, C_{O_2} is the bulk concentration of O₂, D_{O_2} is the O₂ diffusion coefficient in 0.1M KOH, ν is the kinematic viscosity of the electrolyte. The constant 0.2 is adopted when the rotating speed is in rpm.

Rotating ring-disk electrode (RRDE) measurements: The disk electrode was scanned cathodically at a rate of 10 mV s⁻¹ and the ring potential was constant at 1.45 V vs. RHE. The %

HO_2^- and the electron transfer number (n) were determined by the followed equations:

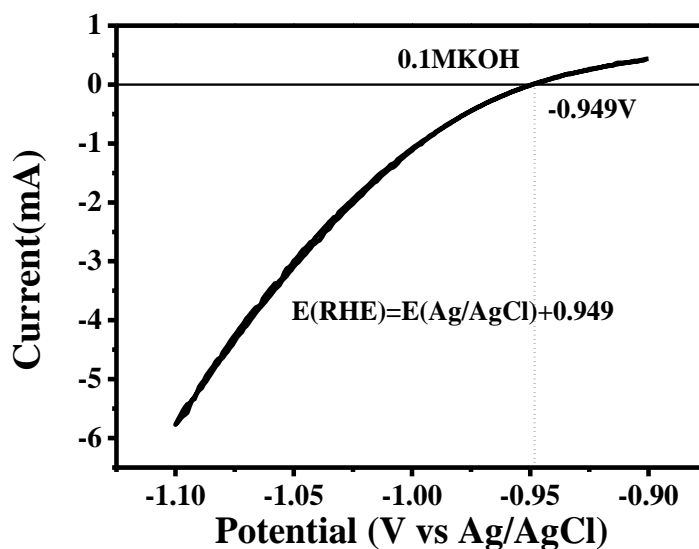
$$n = 4 \times \frac{I_d}{I_d + I_r / N} \quad (3)$$

$$\% \text{HO}_2^- = 200 \times \frac{I_r / N}{I_d + I_r / N} \quad (4)$$

Where I_d is disk current, I_r is ring current and N is current collection efficiency of the Pt ring.

In our system N was determined to be 0.4 from the reduction of $\text{K}_3\text{Fe}[\text{CN}]_6$.

RHE calibration: Ag/AgCl/KCl was used as the reference electrode in all the measurements. It was calibrated with respect to reversible hydrogen electrode (RHE). The calibration was performed in the hydrogen saturated electrolyte with a Pt wire as the working electrode. CVs were carried out at a scan rate of 1mV s^{-1} , and the average of the two potentials at which the current crossed zero was taken to be the thermodynamic potential for the hydrogen electrode reactions.



Preparation of air electrode: 62 mg active carbon, 70 μl PTFE and 8mg catalysts in water and sonicated for two hours respectively, then mixed together and sonicated for another two hours, then centrifuged the composite to get the suspension, washed three times, dried in vacuum at 60

°C for one night. Kneading and rolling the soft powder by adding isopropyl alcohol to get the desired air cathode.

Assemble Zn-air battery: Homemade simple Zn-air battery was used for these experiments. 2 g zinc powder and sodium polyacrylate (0.4%) in 0.6 ml 6M KOH was used as the anode. Cu sheet and Ni foam were used as the current collector. Nylon net filter was used as the separator. Firstly, added the anode to the battery, on the surface of the Zn powder covered the separator. Then catalyst film and Ni foam was put on the top of the separator successively. At last the battery was fixed by screws.

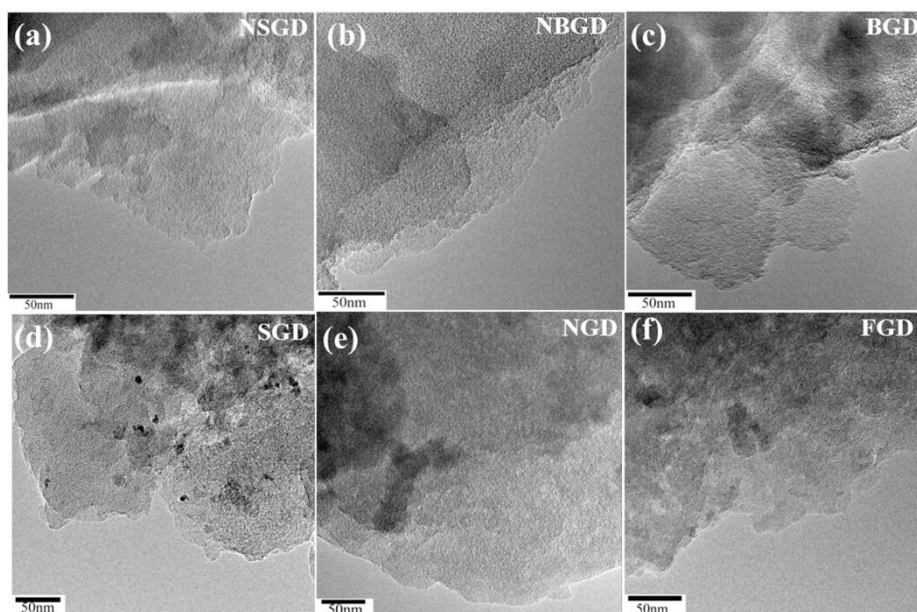


Fig. S1. TEM images of GD, FGD, BGD, SGD and NGD.

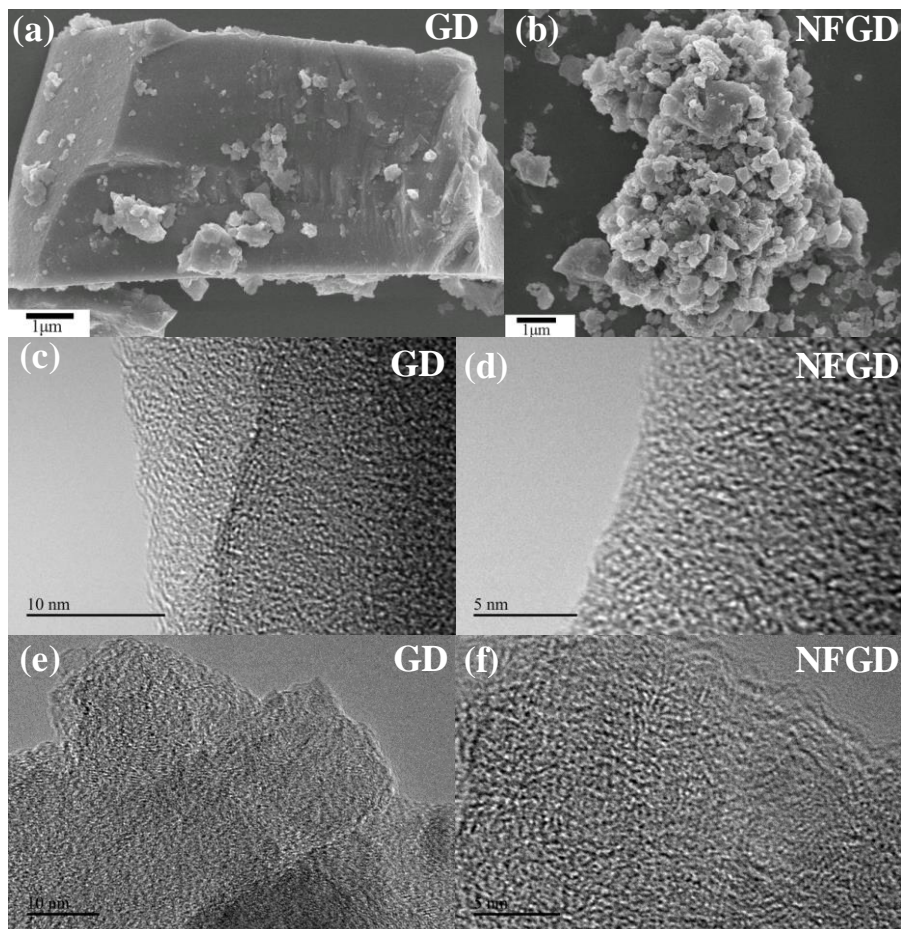


Fig. S2. SEM and HRTEM images of GD and NFGD.

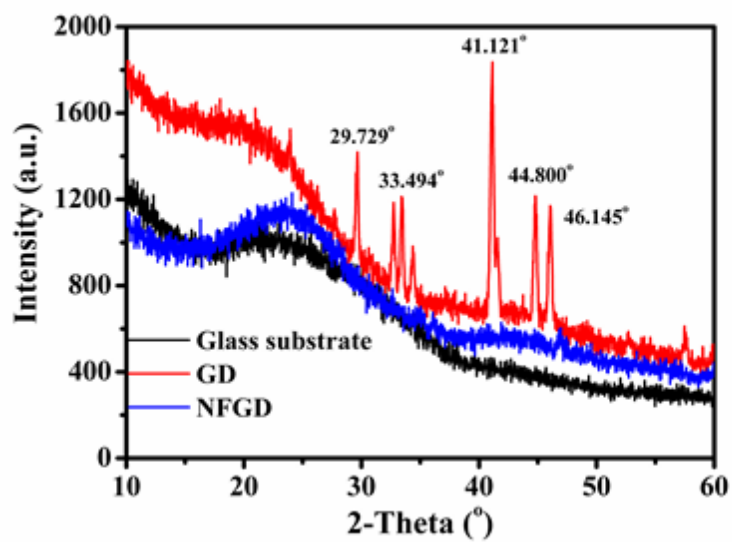


Fig. S3. XRD pattern of glass substrate, GD and NFGD film.

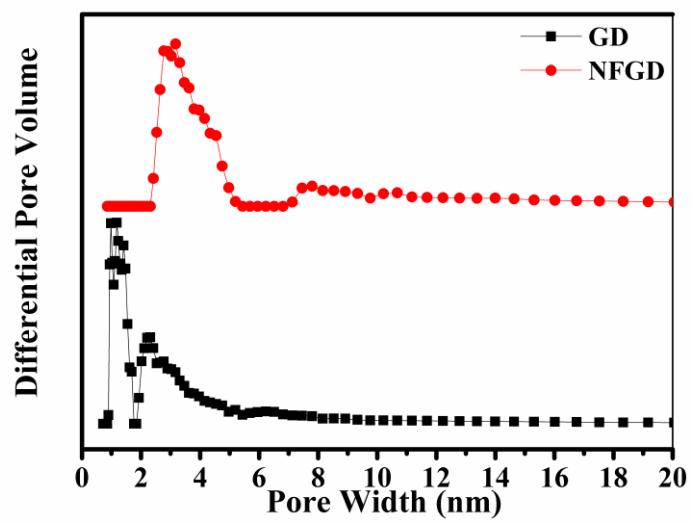


Fig. S4. Pore size distributions of GD and NFGD.

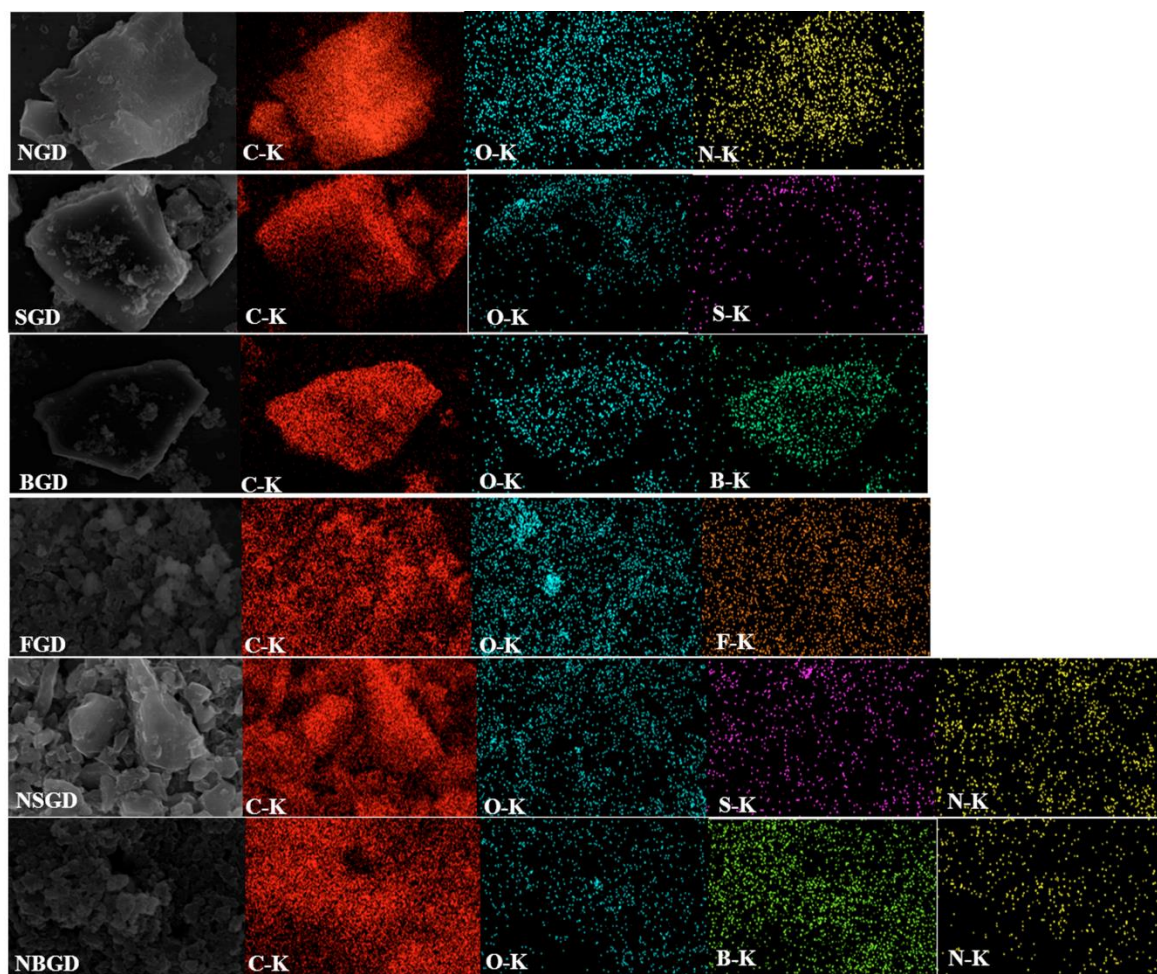


Fig. S5. FESEM images and EDS elemental mapping images of doped-GD materials.

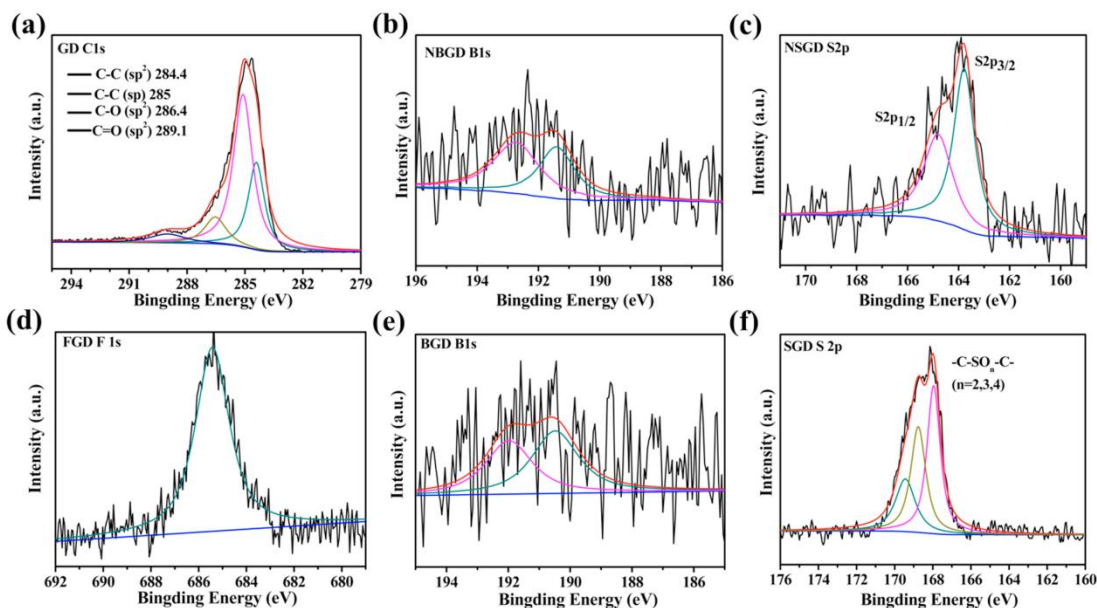


Fig. S6. XPS spectra of GD-based materials. The B1s band can be deconvoluted into two bands at ~ 191.4 , and ~ 192.7 eV, corresponding to the N-B and O-B bonding structures for NBGD, respectively.¹ The peak at ~ 190 and ~ 192.3 eV for BGD corresponds to the structure of C-B and O-B, respectively. In NSGD, the two adjacent peaks at ~ 164.0 and ~ 165.3 eV were assigned to the $-C-S-$ bonds and $-C=S-$ bonds respectively, whereas in SGD, the peaks at the bind energy of around ~ 168 , ~ 169 and ~ 169.8 eV were attributable to $C-SO_x-C$ ($x = 2, 3, 4$).²⁻⁴

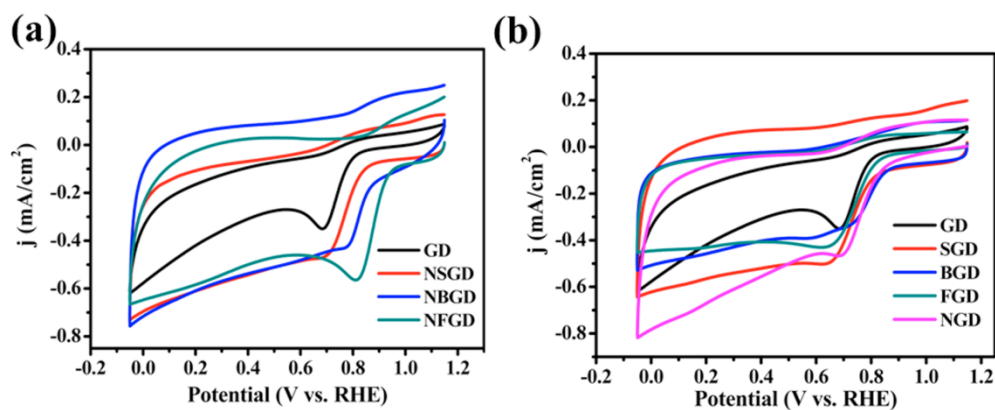


Figure S7. CVs of heteroatoms doped GD materials in O_2 -saturated 0.1M KOH, scan rate: 10mV

s^{-1} .

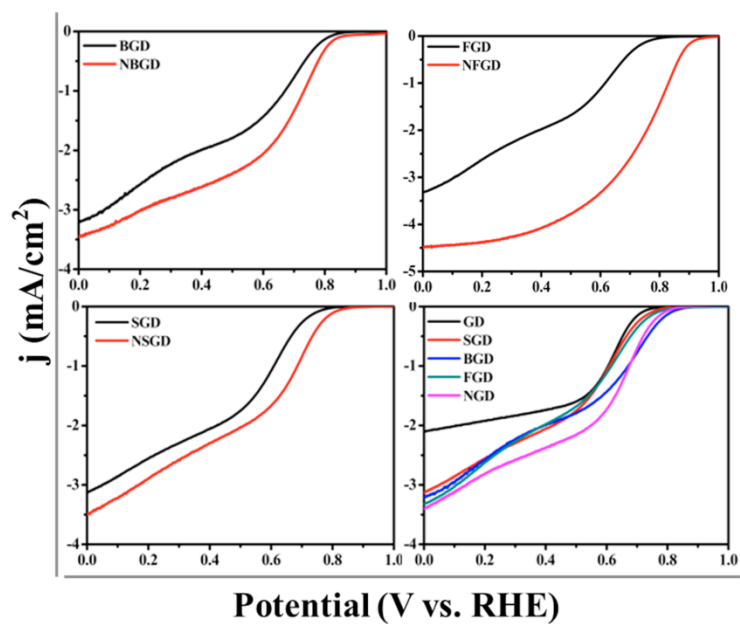


Fig. S8. LSV curves of SGD and NSGD, BGD and NBGD, FGD and NFGD in O_2 -saturated 0.1 M KOH (scan rate: 10 mV s^{-1} ; rotation rate: 1600 rpm).

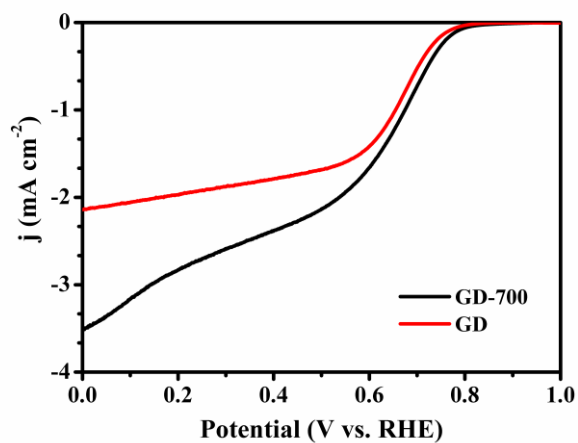


Fig. S9. LSV curves of GD and GD-700 (GD was heated at $700 \text{ }^\circ\text{C}$ under Ar) in O_2 -saturated 0.1 M KOH (scan rate: 10 mV s^{-1} ; rotation rate: 1600 rpm).

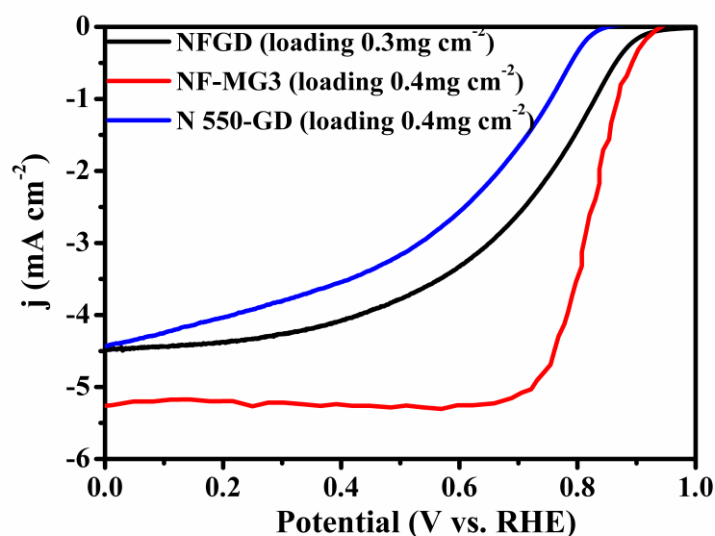


Fig. S10. LSV curves of NFGD (our work), N 550-GD⁵ (our earlier work) and N, F co doped mesoporous graphene⁶ in O₂-saturated 0.1 M KOH. Both the onset potential and half-wave potential of NFGD are more positive shift then N 550-GD, indicating significantly improved catalytic activity toward ORR. The nitrogen and fluorine dual-doped mesoporous graphene (NF-MG3) was synthesized by thermal annealing (900°C) GO/PANI with the aid of NH₄F. Comparing the LSV curves of NFGD and NF-MG3, we can see that they have comparable onset potential. Due to the higher loading of NF-MG3 (0.4 mg cm⁻²) and 900°C heating treatment, it shows a higher limiting current density and positive half-wave potential.

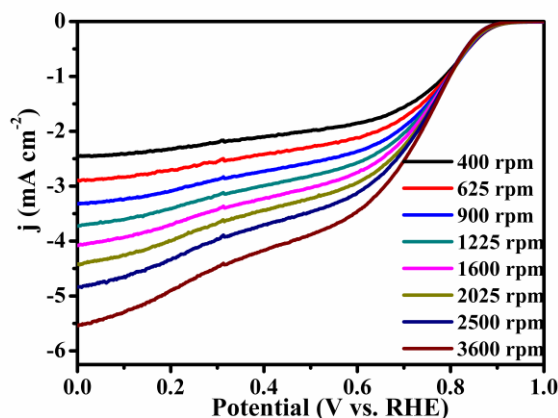
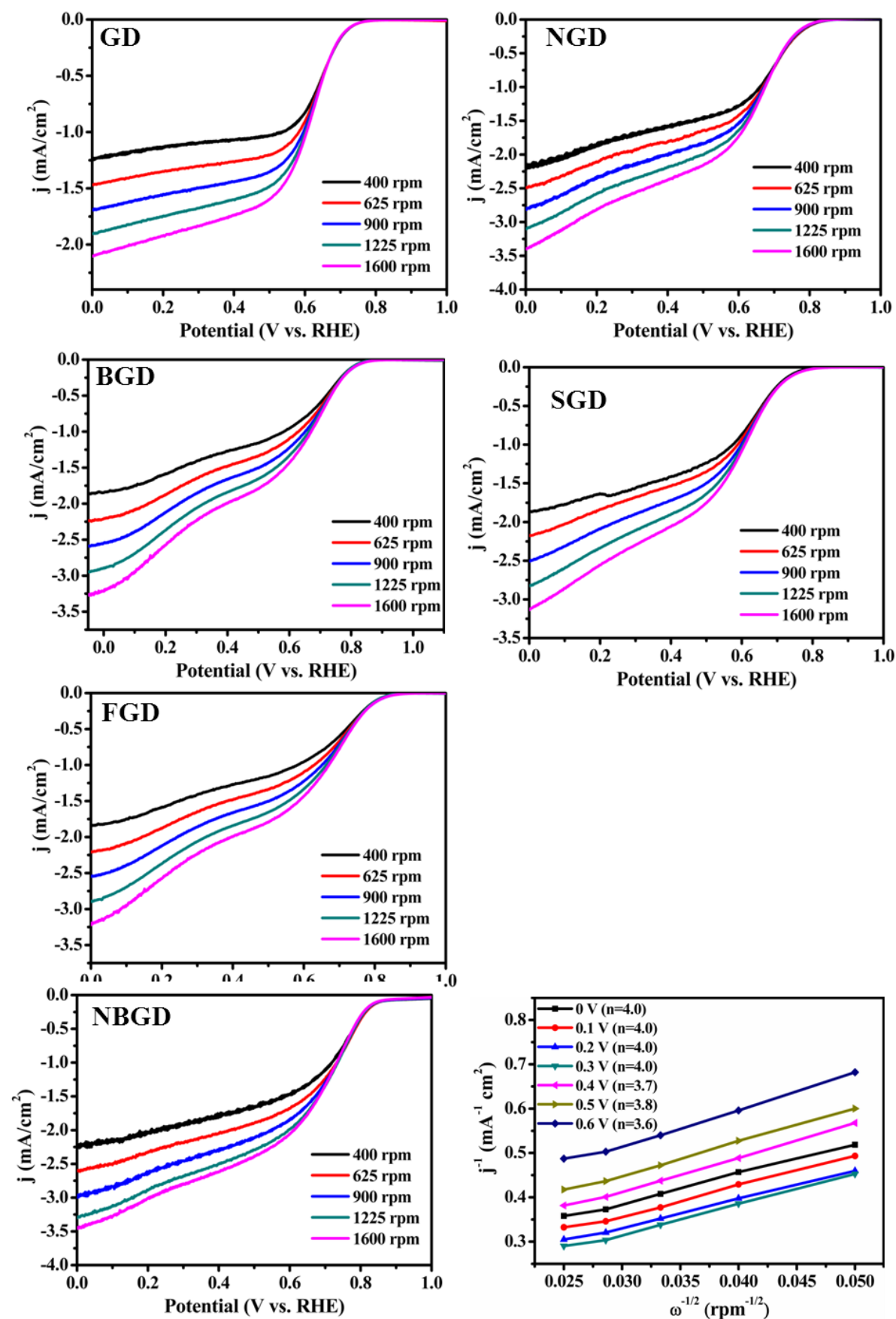


Fig. S11. LSV curves of NFGD in O₂-saturated 0.1 M KOH (scan rate: 10 mV s⁻¹; rotating rate:

400 rpm -3600 rpm).



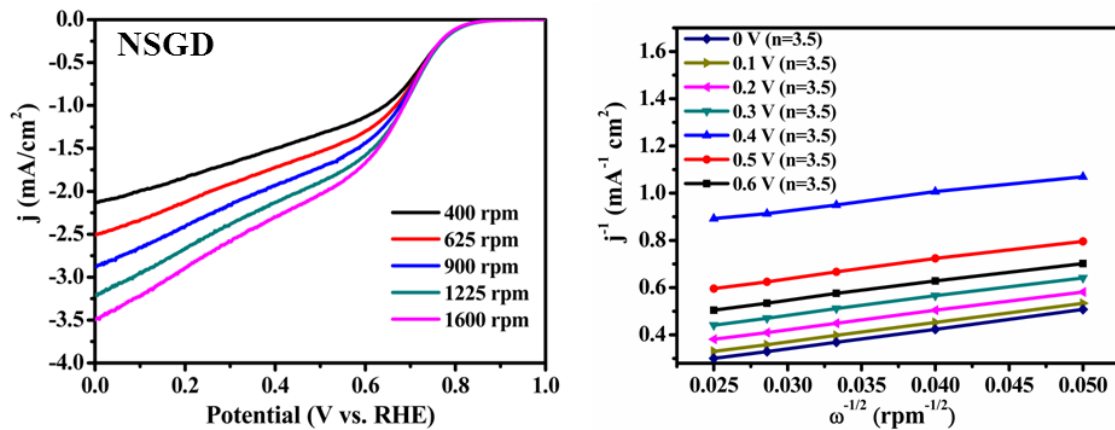


Fig. S12. Linear sweep voltammograms (LSV) curves of GD, NGD, SGD, BGD and FGD obtained from the RDE tests at different rotating rates (400~1600 rpm) in O₂-saturated 0.1M KOH solution and the K-L plots calculated from the LSV curves.

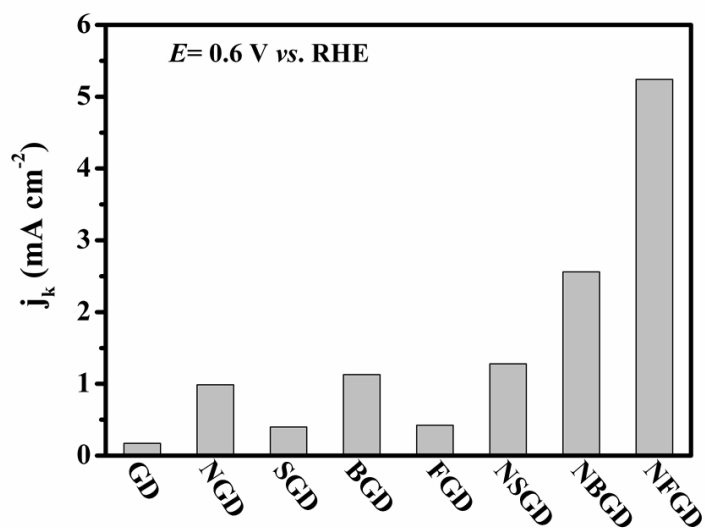


Fig. S13. j_k of different catalysts calculated at the potential of 0.6 V vs. RHE. Limiting current density obtained at potential 0.2 V vs. RHE was used to calculate j_k using the equations,

$$j_k = \frac{j j_D}{j_D - j}$$

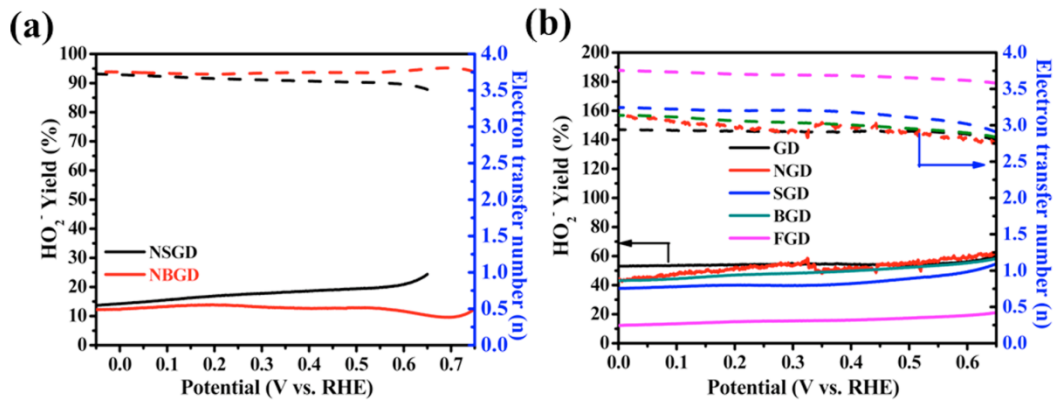


Fig. S14. The variations of the HO_2^- yield and the electron transfer number at various disk electrode potential during the ORR.

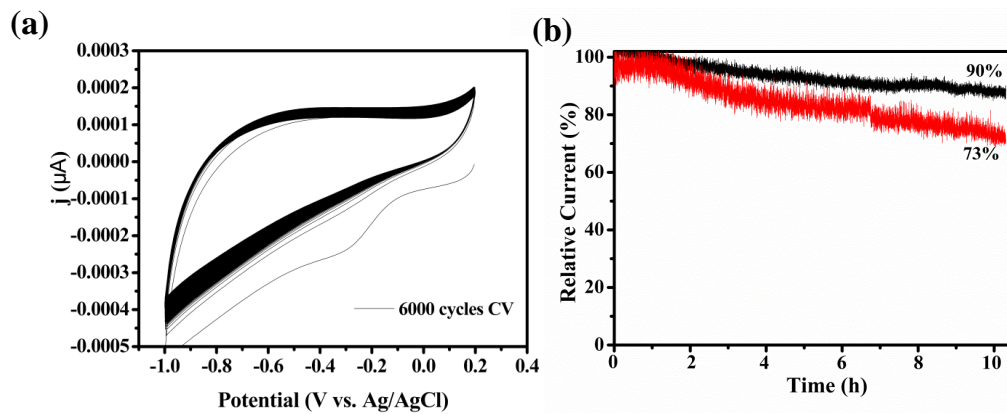


Fig. S15. (a) CVs during 6000 cycles in O_2 -saturated 0.1M KOH (200 mV s^{-1} for 12000 segments); (b) durability evaluation of NFGD and Pt/C electrodes for more than 10 h at 0.6V vs. RHE.

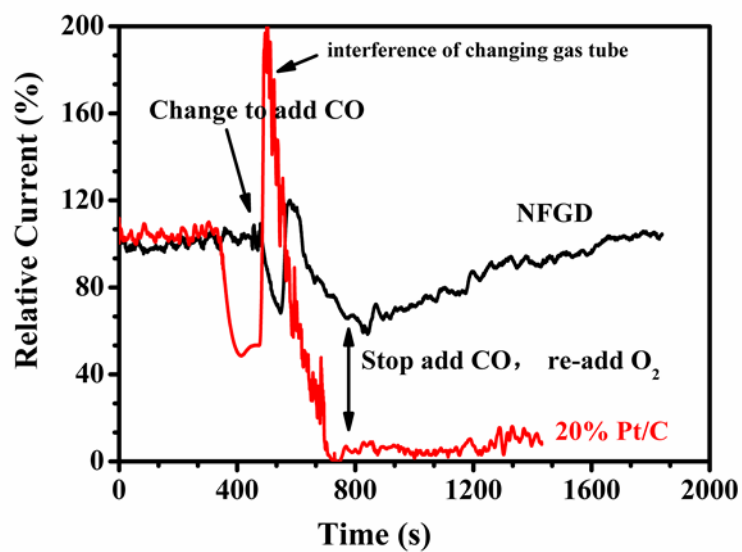


Fig. 16. Carbon monoxide of NFGD compared with 20% Pt/C electrocatalysts at 0.6V (vs. RHE).

First add O₂ to the electrolyte, and then CO was added to the electrolyte at the time of 500s and stopped at the 800s and add O₂ again.

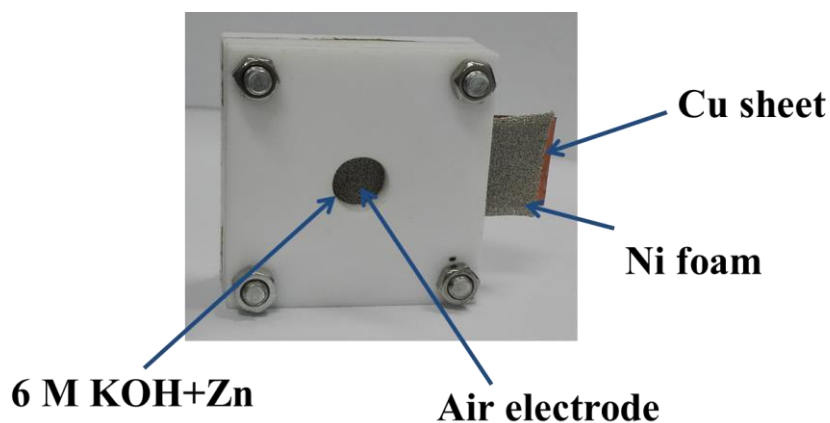


Fig. S17. Digital photograph of homemade primary Zn-air battery.

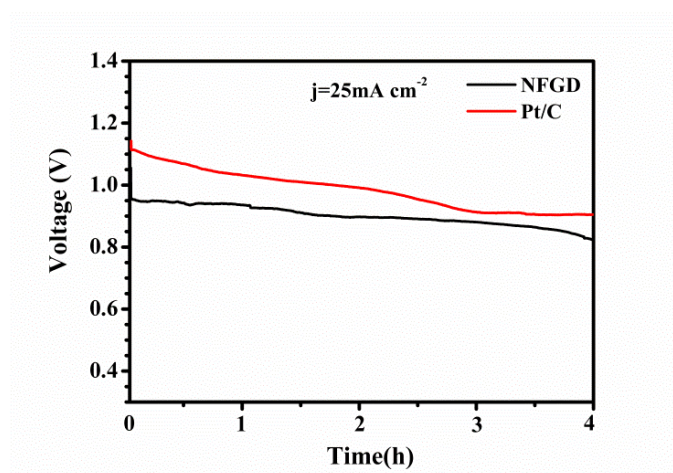


Fig. S18. Typical galvanostatic discharge curves of Zn-air cells with NFGD and Pt/C as cathode catalysts at 25 mA cm⁻². No obvious voltage drop was observed from the long-term galvanostatic discharge curves after continuous discharge for 4 hours.

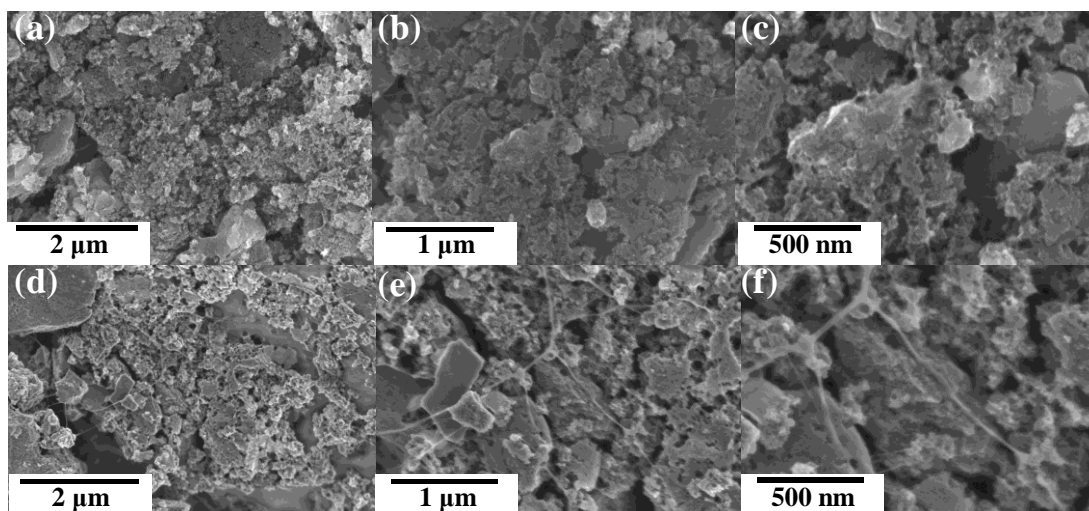


Fig. S19. SEM images of catalyst films before (a-c) and after discharge (d-f).

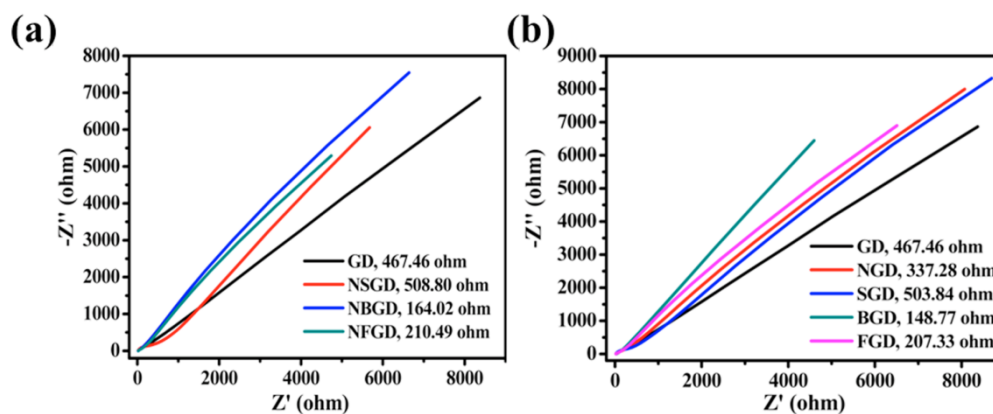


Fig. S20. Nyquist plots of GD-based materials. The Nyquist plots reveal that the resistance of GD-based materials highly depends on the heteroatom dopant. While the doping of S even makes the resistances of the SGD and NSGD electrodes higher (503.84 Ω and 508.8 Ω), the doping of N or B or F endows the corresponding electrodes with a small series resistance favorable for electron transfer.

Table S1. The ratios of different elements in GD-based materials obtained from the XPS results.

Catalysts	C%	O%	N%	S%	B%	F%
GD	87.52	12.48	/	/	/	/
NGD	86.57	6.49	6.93	/	/	/
SGD	79.26	19.44	/	1.3	/	/
BGD	88.79	10.97	/	/	0.24	/
FGD	72.29	19.15	/	/	/	0.8
NSGD	75.28	9.26	14.8	0.57	/	/
NBGD	80.02	15.13	4.62	/	0.59	/
NFGD	76.04	16.51	4.45	/	/	0.3

Table S2. I_D/I_G ratio of GD-based catalysts obtained from the Raman spectra.

Catalysts	Intensity of D bands (a.u.)	Intensity of G bands (a.u.)	I_D/I_G
GD	1846.84	2498.97	0.74
NGD	21075.19	23374.78	0.90
SGD	15159.45	15773.84	0.96
BGD	11921.59	12534.81	0.95
FGD	10791.69	10255.12	1.0
NFGD	7905.79	6448.80	1.22
NBGD	6372.73	6485.95	0.98
NSGD	5287.30	4679.05	1.13

Table S3. Summary of ORR performances on GD-based catalysts obtained from LSV in 0.1M KOH, with 20% Pt/C as comparison. The electron transfer number and HO_2^- yield were got at 0.6V vs. RHE.

Catalysts	E_{onset} (V vs.RHE)	i_d (mA cm ⁻²)	Electron transfer number	HO ₂ ⁻ yield
GD	0.80	2.1	2.9	56
NGD	0.87	3.3	2.8	59
SGD	0.84	3.0	3.0	49
BGD	0.85	3.1	2.9	55
FGD	0.84	3.2	3.6	19
NSGD	0.89	3.4	3.6	20.8
NBGD	0.90	3.4	3.7	11.6
NFGD	1.0	4.5	3.8	11.3
Pt/C	1.0	4.3	3.9	6.3

Table S4. Comparison of the performances between NFGD (this work) and other heteroatoms doped metal-free catalysts catalyze ORR in alkaline media reported in the literatures.

Catalysts	E_{onset} (V vs. RHE)	$E_{half-wave}$ (V vs.RHE)	i_d (mA cm ⁻² , 0 V)	E_{peak} (V vs. RHE)	References
N, F-codoped graphdiyne	1.0	0.74	4.5	0.81	This work
N, B-codoped graphene	0.88	0.7	5.01	0.7	<i>Angew. Chem.Int. Edd.</i> 2013, 52, 3110
N, S-codoped graphene	0.86	0.65	2.1	0.7	<i>Adv. Mater.</i> 2014, 26, 6186
N, O-codoped mesoporous carbon	0.86	0.70	4.0	0.7	<i>J. Am. Chem. Soc.</i> 2013, 135, 7823
N, P-codoped hierarchical porous carbon foams	0.88	0.75	5.5	0.72	<i>Chem. Eur. J.</i> 2014, 20, 3106
I-doped graphene	0.88	0.72	7.0	0.68	<i>Chem. Commun.</i> 2012, 48, 1027
F, Cl-codoped graphene	0.85	0.68	5.1	0.64	<i>Electrochimica Acta</i> 177 (2015) 36
N, F-codoped mesoporous graphene	1.047	0.828	5.2	0.803	<i>Nanoscale</i> , 2015, 7, 10584

Computational Calculation Section:

Models and Method:

The geometries of the GD-based materials were optimized by density functional theory (DFT) calculations with the B3PW91 functional and 6-31G** basis set. Based on the optimized geometries, the atomic charges were calculated by natural population analyses at the same level of theory. The respective binding energies were obtained with calculations corrected for the basis set superposition error. All the calculations were carried out using the Gaussian 09 package. With respect to the experimental values, the calculated B 1s, S 2p and F 1s binding energies in the gas

phase are underestimated, this could be due to the lack of polarization presented in solid-state films.

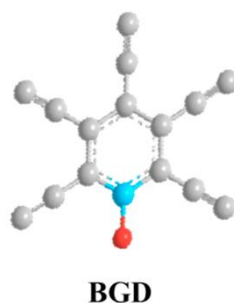


Fig. S21. Models for B doping sites in BGD. Colour codes: grey is carbon, blue is boron and red is oxygen.

Since B can only form C-B and B-O bonds (XPS examination) in BGD, the doping site for B is on the edge of such GD model.

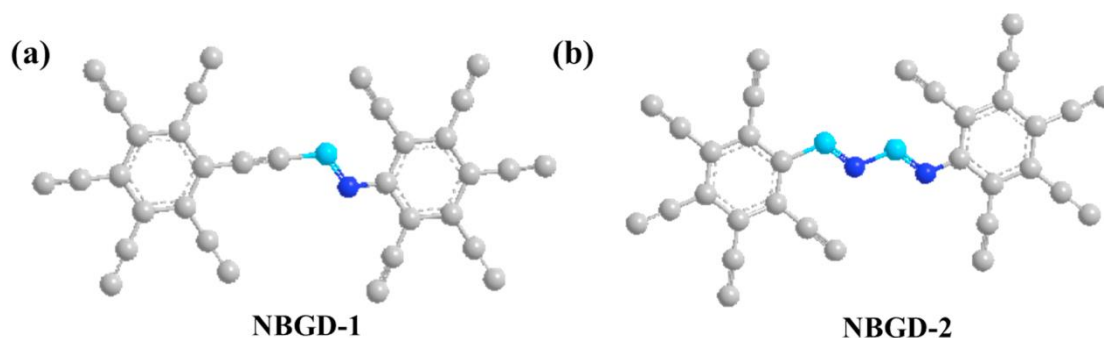


Fig. S22. Models for N and B doping sites in NBGD. Colour codes: grey is carbon, blue is boron and dark blue is nitrogen.

As the main form for B in NBGD is N-B bonds, the doping sites for B in NBGD could be the linear atomic chains between two carbon hexagons as shown in Figure S13. Earlier calculations have proven that the BN unit preferred to replace the sp-hybridized carbon atoms in the chain at a low doping rate,⁷ forming a N-B-N-B- bridge between two carbon hexagons. Moreover, a much higher B atomic percentage in NBGD than those observed for BGD was identified, which

suggests the interaction between N and B and thereby supports the calculation results.

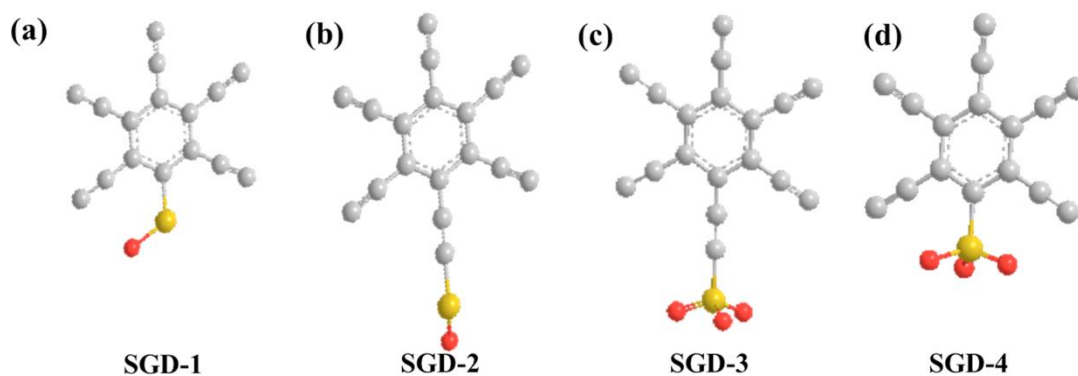


Fig. S23. Models for S doping sites in SGD. Colour codes: grey is carbon, yellow is sulfur and red is oxygen.

In SGD, S can only form $-\text{SO}_x-$ bond, our result show that the doping sites for S are main at the C-C single bonds in the linear chains.

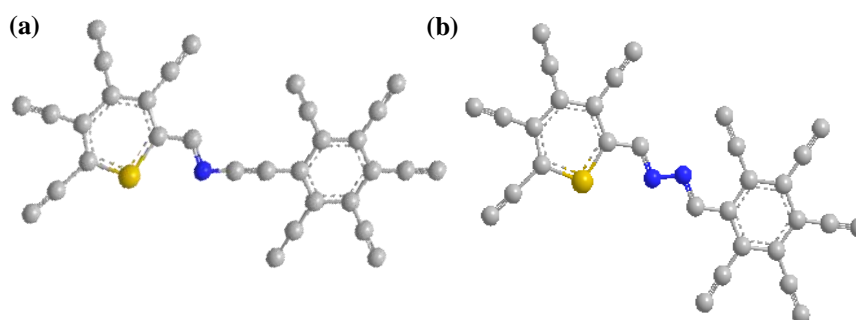


Fig. S24. Models for N, S doping sites in NSGD. Colour codes: grey is carbon, yellow is sulfur and dark blue is N.

Since S can only form double bond with C (XPS examination) in NSGD, the doping site for S is on the edge of such GD cluster model.

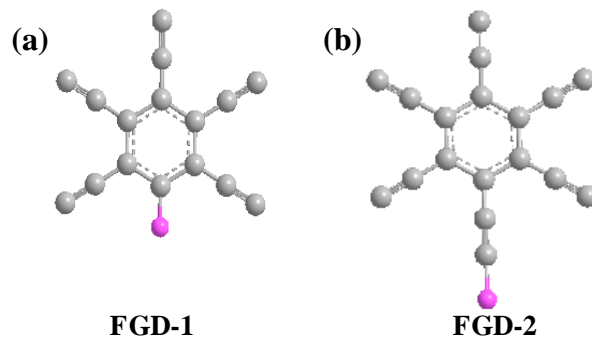


Fig. S25. Models for F doping sites in FGD. Colour codes: grey is carbon, pink is fluorine.

As F can only form single ionic C-F bonds (XPS examination) both in FGD and NFGD, the replacement could be achieved at the two C-C single bonds in chains. The theoretical XPS F 1s values (Table S5) calculated by the DFT on the basis of the two model shown that the F1s value of FGD-1 match well with that of our experimental XPS results.

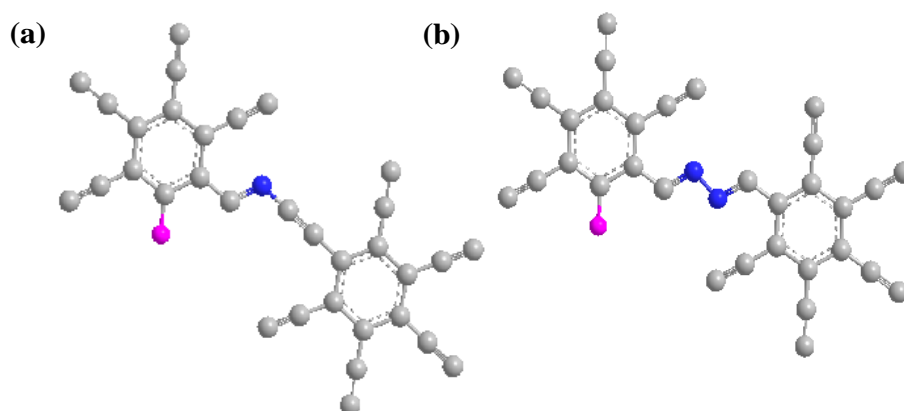


Fig. S26. Models for N, F doping sites in NFGD. Colour codes: grey is carbon, dark blue is nitrogen, pink is fluorine.

Charge density distributions:

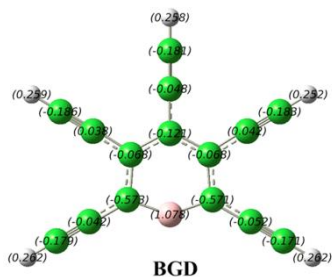


Fig. S27. DFT-calculated charge density distributions for the BGD. Colour codes: green is carbon, light red is boron, grey is hydrogen.

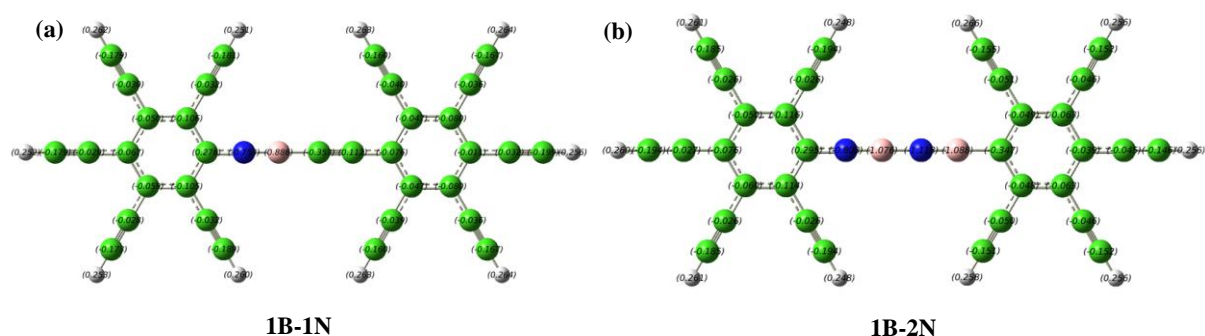


Fig. S28. DFT-calculated charge density distributions for the NBGD. Colour codes: green is carbon, dark blue is nitrogen, light red is boron, grey is hydrogen.

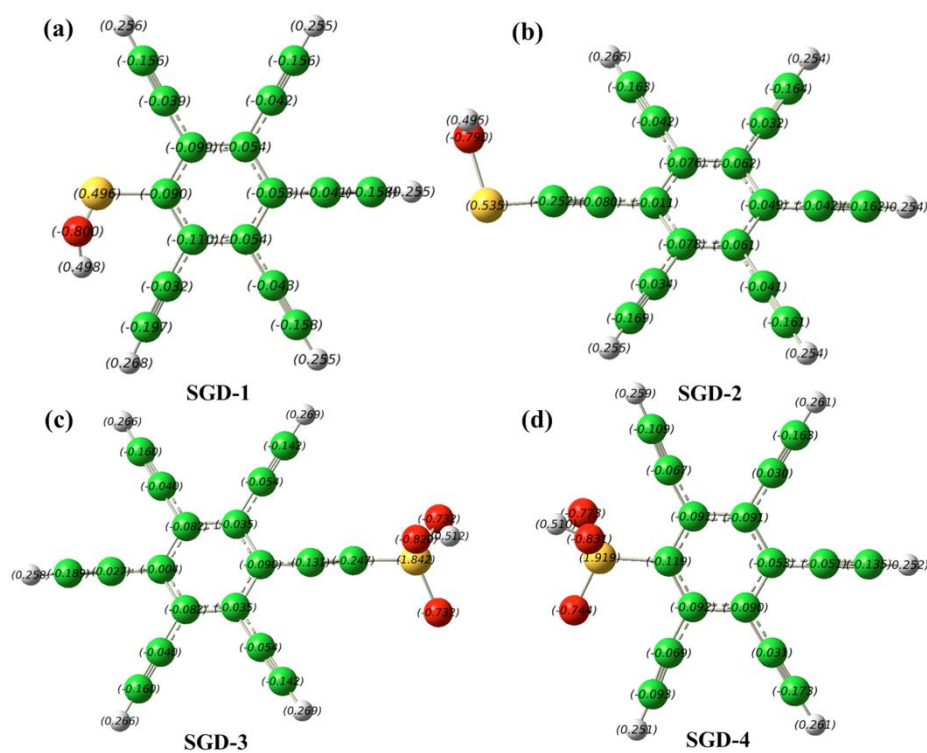


Fig. S29. DFT-calculated charge density distributions for the SGD. Colour codes: green is carbon, yellow is boron, red is oxygen, grey is hydrogen.

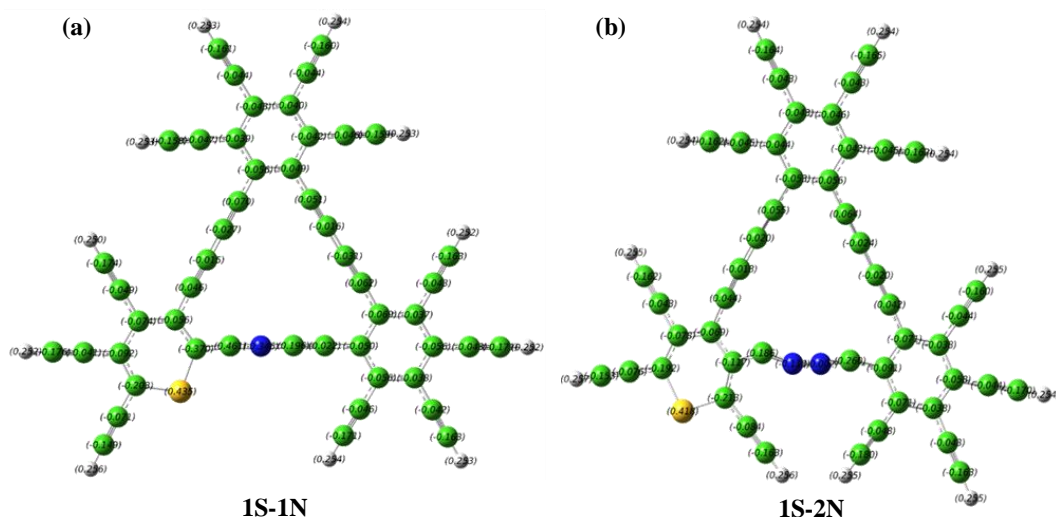


Fig. S30. DFT-calculated charge density distributions for the NSGD. Colour codes: green is carbon, dark blue is nitrogen, yellow is sulfur, grey is hydrogen.

Table S5. DFT-calculated heteroatoms binding energies (eV) for the GD-based materials.

Molecule	Orbital	Binding energy (eV)
BGD	B 1s	182.2
SGD-1	S 2p (x, y, z)	162.4,162.4,162.1
SGD-2	S 2p (x, y, z)	162.7,162.4,162.7
SGD-3	S 2p (x, y, z)	168.2,168.1,168.2
SGD-4	S2p (x, y, z)	168.0,168.1,168.1
FGD-1	F 1s	664.9
FGD-2	F 1s	666.9
1B-1N	B 1s	181.2
1B-2N	B 1s	181.2
1S-1N	S 2p (x, y, z)	161.6, 161.6, 161.4
1S-2N	S 2p (x, y, z)	161.8, 161.8, 161.6
1F-1N	F 1s	665.6
1F-2N	F 1s	665.0

Reference

1. W. B. Wan and M. M. Haley, *The Journal of organic chemistry*, 2001, **66**, 3893-3901.
2. M. M. Haley, *Pure Appl Chem*, 2008, **80**, 519-532.
3. D. Malko, C. Neiss, F. Viñes and A. Görling, *Physical review letters*, 2012, **108**, 086804.
4. X. Wang, J. Wang, D. Wang, S. Dou, Z. Ma, J. Wu, L. Tao, A. Shen, C. Ouyang and Q. Liu, *Chemical Communications*, 2014, **50**, 4839-4842.
5. R. Liu, H. Liu, Y. Li, Y. Yi, X. Shang, S. Zhang, X. Yu, S. Zhang, H. Cao and G. Zhang, *Nanoscale*, 2014, **6**, 11336-11343.
6. Y. Sun, H. Dai, J. Hu, P. Ni, Y. Wang, Z. Li and Z. Li, *Nanoscale*, 2015.
7. H. Bu, M. Zhao, H. Zhang, X. Wang, Y. Xi and Z. Wang, *J Phys Chem A*, 2012, **116**, 3934-3939.